Nano Energy 97 (2022) 107159

Contents lists available at ScienceDirect

Nano Energy

journal homepage: www.elsevier.com/locate/nanoen

Lever-inspired triboelectric nanogenerator with ultra-high output for pulse monitoring

Maoyi Zhang [a,b,d], Wenxuan Zhu [a,c], Tongtong Zhang [a,c], Yewang Su [b,d,*], Ya Yang [a,c,**]

[a] CAS Center for Excellence in Nanoscience, Beijing Key Laboratory of Micro-Nano Energy and Sensor, Beijing Institute of Nanoenergy and Nanosystems, Chinese Academy of Sciences, Beijing 101400, China
[b] State Key Laboratory of Nonlinear Mechanics, Institute of Mechanics, Chinese Academy of Sciences, Beijing 100190, China
[c] School of Nanoscience and Technology, University of Chinese Academy of Sciences, Beijing 100049, China
[d] School of Engineering Science, University of Chinese Academy of Sciences, Beijing 100049, China

ARTICLE INFO

Keywords:
Lever-inspired
Triboelectric nanogenerator
Pulse sensor
Charge transfer speed

ABSTRACT

Triboelectric nanogenerators (TENGs) have great potential to alleviate the energy crisis. The contact separation mode of TENGs is one of the most fundamental and common modes of working. For improving the output signal of contact separation TENGs, previous researchers have adopted strategies such as surface microstructure treatment, multilayer design, and additive pump design. All of these strategies aim to increase the surface charge. Here, we propose a new strategy aimed at increasing the charge transfer speed, provide new paths for improving the output signal, and develop a lever-inspired contact separation TENG (Li-TENG). The contact separation speed can be varied by changing the lever ratio. As the magnification increases from 22 to 50 times, the voltage of Li-TENG increases from 91 V to 232 V. As self-powered pulse sensor, the Li-TENG measured a pulse signal of 12.3 V without surface microstructure treatment. This work shows great potential for improving the signal of contact-separation TENG-based self-powered sensors and energy harvesting devices.

1. Introduction

Recently global energy has become increasingly scarce. Triboelectric nanogenerators (TENGs), first proposed in 2012 [1], can collect mechanical energy extensively through contact initiation and electrostatic induction, and have great potential in alleviating the energy crisis. After some years of development, TENGs have shown a wide range of applications in self-powered sensors [2] and mechanical energy harvesting [3]. TENGs have four basic modes of working: lateral sliding mode [4,5], contact-separation mode [6–10], freestanding triboelectric-layer mode [11–13], and single-electrode mode [14,15]. Due to the advantages of high instantaneous output power, simple preparation and design, and easy multilayer integration, the contact-separation mode has become one of the most fundamental and common modes of working.

Many works have been made by previous researchers for improving output signal of contact-separation TENGs. For example, for increasing the surface charge density, it is common to microstructure the friction layer surface [16–19]. For contact-separation TENGs with abundant space, multilayer designs have also been used to increase the area for storing charge [20–24]. Another recent novel approach is adding a pump to the TENG for overcoming the limitation of the maximum surface charge density of the friction layer [25–28]. The strategies mentioned above are all aimed at increasing the surface charge. The magnitude of the output signal is related not only to the amount of charge transfer but also to the charge transfer speed.

Here, we propose a new strategy aimed at increasing the charge transfer speed, provide new paths for improving the output signal, and develop a lever-inspired contact separation TENG (Li-TENG). By varying the lever ratio to change the contact separation velocity, the signal output can be significantly increased without changing the charge transfer amount. To accommodate the unique rotational motion of the lever, we designed the upper friction layer in the curved shape and investigated the electrical and mechanical properties of the curved-shaped friction layer under different compression strains. When the magnification was increased from 22 to 50 times, the voltage of Li-TENG increased from 91 to 232 V and the maximum power from 83 to 1031

* Corresponding author at: State Key Laboratory of Nonlinear Mechanics, Institute of Mechanics, Chinese Academy of Sciences, Beijing 100190, China.
** Corresponding author at: CAS Center for Excellence in Nanoscience, Beijing Key Laboratory of Micro-Nano Energy and Sensor, Beijing Institute of Nanoenergy and Nanosystems, Chinese Academy of Sciences, Beijing 101400, China.
E-mail addresses: yewangsu@imech.ac.cn (Y. Su), yayang@binn.cas.cn (Y. Yang).

https://doi.org/10.1016/j.nanoen.2022.107159
Received 21 February 2022; Received in revised form 11 March 2022; Accepted 16 March 2022
Available online 19 March 2022

μW. As self-powered pulse sensor, the Li-TENG measured a pulse signal of 12.3 V without surface microstructure treatment, which is much higher than other literature [16–18,29–37]. This work demonstrates a new strategy for improving the signal of contact-separation TENGs, which has great potential for improving the signal of contact-separation TENG-based self-powered sensors and energy harvesting devices.

2. Experimental section

2.1. Fabrication of Li-TENG

The main bar made of Stereolithography (SLA) material was produced using 3d printing (Mohou Co. Ltd., China). The geometry dimensions of the main bar are shown in Fig. S1. The holder and other accessories were made by laser cutting acrylic (PLS4.75, General laser Systems, USA). The main bar and the holder are connected with bearings and acrylic glue. A layer of silver (Ag) electrode was sputtered on a 25 mm × 25 mm × 50 μm Polyimide (PI) film using magnetron sputtering, and a layer of 25 mm × 25 mm × 50 μm fluorinated ethylene propylene (FEP) film with adhesive on one side was glued on top of the Ag electrode. The curved upper friction layer was obtained by fixing the pre-compressed PI-Ag-FEP at both ends with double-sided adhesive on the acrylic plate. The lower friction layer was obtained by gluing a 35 mm × 35 mm × 20 μm aluminum (Al) foil to the 35 mm × 35 mm × 3 mm foam with double-sided adhesive, and then gluing a 35 mm × 35 mm × 50 μm Nylon film with adhesive to the Al foil. The upper friction layer and the lower friction layer were mounted on the main bar and the holder respectively with acrylic bolts and nuts.

2.2. Characterization and measurements

A mixed domain oscilloscope (Tektronix MDO3024) with a 100 MHz high voltage differential probe (Tektronix THDP0100) was employed to measure the voltage of the Li-TENG. Movement of the upper friction layer and Li-TENG is controlled by a linear motor (Linmot E1100).

2.3. Finite element analysis (FEA) simulation

ABAQUS was selected to analyze the bending of the main bar of Li-TENG and the uniaxial compression behavior of the upper friction layer. SLA and PI were treated as linear elastic material with their elastic modulus and Poisson's ratio of 2.6 GPa, 0.34, 2.5 GPa, 0.34, respectively. FEP was treated as an ideal elastic plastic material, whose elastic modulus, Poisson's ratio and yield stress were 480 MPa, 0.4 and 12 MPa respectively. SLA adopted the hexahedron elements C3D8R, and PI and FEP adopted the shell element S4R.

3. Results and discussion

3.1. Fabrication and working mechanism of Li-TENG

We assembled a Li-TENG that can be used for pulse measurement, which is shown schematically and physically in Figs. 1a and S2, respectively. Laser-cut acrylic was used as the holder. 3D printed SLA was used as the main bar. The holder and the main bar were connected to each other with a pivot point assembled by a bearing. The front end of the main bar is used as the driving end and is in contact with the object under test. A spring (~0.18 N/mm) was installed between the main bar and the holder near the pivot point. An upper friction layer and a lower friction layer are installed at the end of the main bar and the end of the holder, respectively. The upper friction layer is divided into three layers, the upper is the support layer made by PI film, the middle is the conductive layer made by Ag electrode, and the lower is the friction layer made by FEP film. The lower friction layer is divided into three layers, the upper is the friction layer made by Nylon film, the middle is the conductive layer made by Al foil, and the lower is the buffer layer

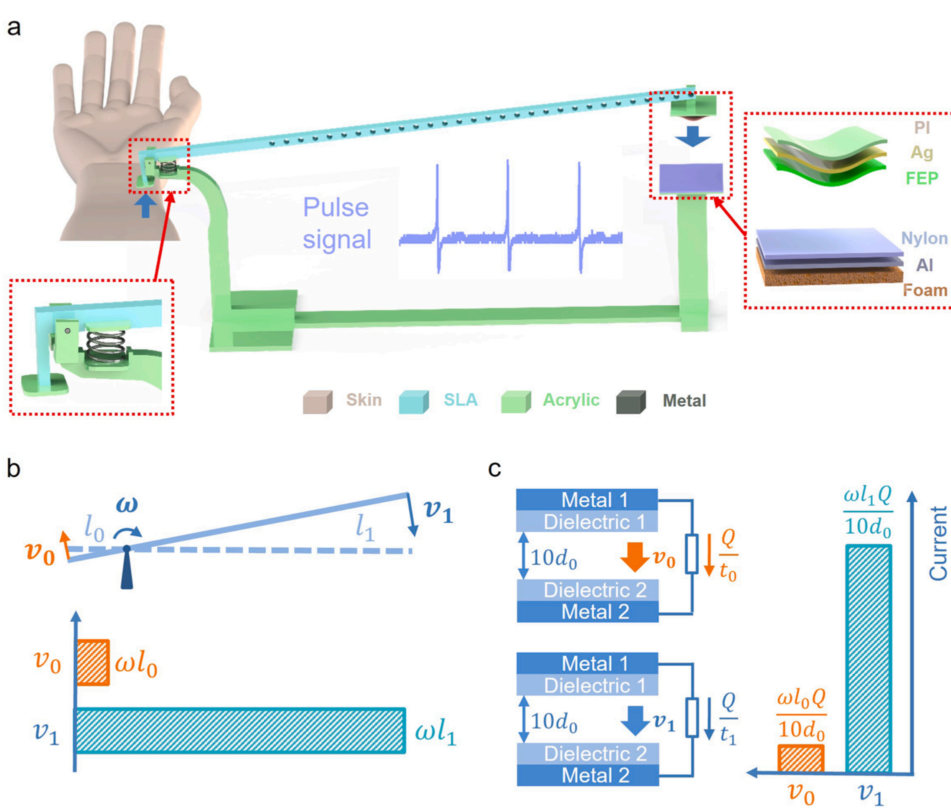

Fig. 1. Model diagram and schematic diagram of Li-TENG. (a) Model diagram of Li-TENG. (b) Schematic diagram of angular velocity. (c) Schematic diagram of TENG current.

made by foam.

As shown in Fig. 1b, the lever rotates around the fulcrum with an angular velocity ω. The distance of the front end from the fulcrum is l_0. And l_0 is a constant value equal to 5 mm. The distance of the end from the fulcrum is l_1. Then the magnitudes of the front-end velocity $\boldsymbol{v_0}$ and the end velocity $\boldsymbol{v_1}$ are ωl_0 and ωl_1, respectively. Thus, the lever can amplify the velocity by a factor of $l_1/\ l_0$. The contact separation TENG has a characteristic that its short-circuit transfer charge has a tendency to saturate. When the separation distance between the upper and lower friction layers increases from 0 to 10 d_0, the short-circuit transfer charge will be a rapid increase to 90% of the saturation value. d_0 is the sum of the ratio of the thickness of all the dielectric materials between the two electrodes and their relative dielectric constants, which belongs to the same order of magnitude as the thickness of the friction materials. For ease of understanding, we have simplified here by treating the transferred charge Q as a constant value that does not vary with time. The current is the ratio of the transferred charge and the time, so increasing the speed of motion can increase the current (Fig. 1c). The voltage except for the open circuit voltage is proportional to the current. Therefore, the lever structure design can significantly increase the current and the voltage except for the open circuit voltage. For the convenience of the description, the voltage except for the open circuit voltage is referred to as the voltage in the following. In fact, the transferred charge Q is a function about time, which was derived in detail by Niu et al. [38]. They found that the short-circuit current is linearly and positively related to the speed. During the actual measurement, the

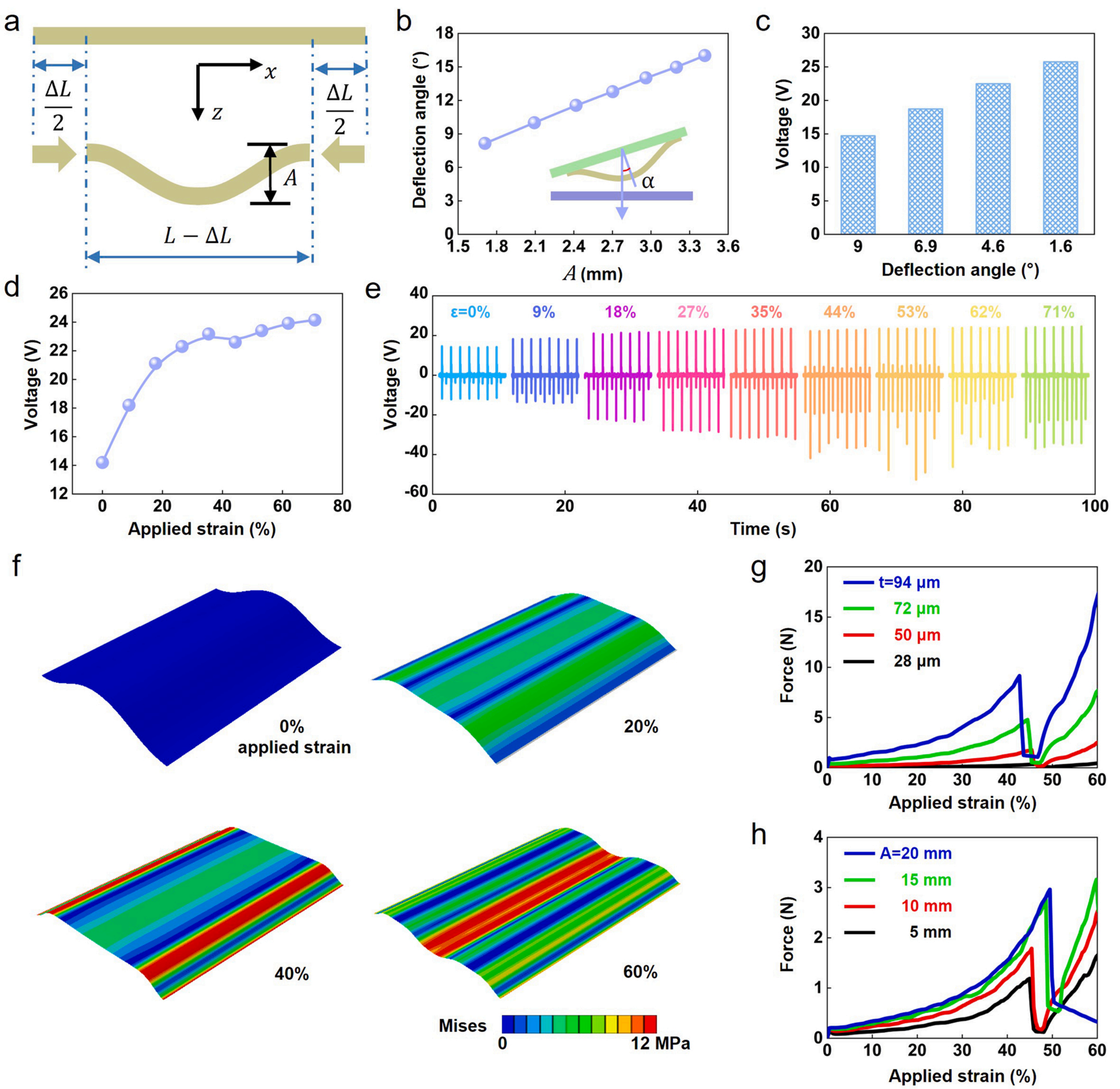

Fig. 2. Electrical testing and mechanical analysis of curved friction layers. (a) Geometric configuration of the curved friction layer. (b) Relationship between deflection angle and amplitude. Voltage signals at (c) different deflection angles and (d) different applied strains. (e) Voltage waveform signals under different strains. (e) Stress distributions of curved friction layer under different strains by FEA. Force-strain curves at (g) different PI thicknesses and (h) different amplitudes of the curved friction layer.

small resistance load is also considered as a short-circuit current [39]. The current in this case is also positively correlated with the speed. Although the relationship between current and speed changes as the resistance increases. During the actual measurement, the current under the small resistance load is also considered as short-circuit current. The current in this case is also positively correlated with the speed. Although the relationship between current and speed changes as the resistance load increases, we infer that there must exist a certain range under which the current is positively correlated with the speed. This is confirmed by the experiments later in this paper.

3.2. Electrical performance and mechanical analysis of curved friction layers

According to the principle of TENG, voltage and contact area are positively correlated. The motion of the lever structure is a rotary motion, not a conventional vertical motion. If the shape of both friction layers is planar, then only at a specific angle of rotation will there be face-to-face contact, in all other cases it will be line-to-surface contact, and the contact area under line-to-surface contact will be almost zero. In order to enable Li-TENG to achieve face-to-face contact within the wide range of deflection angles without external adjustment, we designed one of the friction layers - the upper friction layer - as a curved structure, as shown in Fig. 2a. The upper friction layer of original length L is fixed at both ends and subjected to compression at a distance of ΔL, and the overall buckling occurs. Its vertical displacement w and horizontal displacement u are shown in Eq. (1) [40,41],

$$\begin{cases} w = \dfrac{A}{2}\left(1 + \cos\dfrac{2\pi x}{L}\right) \\ u = \dfrac{\pi A^2}{16L}\sin\dfrac{4\pi x}{L} - \dfrac{\Delta L}{L}x \end{cases} \tag{1}$$

where $A = (2/\pi)\sqrt{\varepsilon_{applied}}, \varepsilon_{applied} = \Delta L/L$ is the applied strain. The allowed deflection angle α varies at different amplitude A. The amplitude A is varied by changing the applied strain with the same original length of the upper friction layer. Fig. 2b shows the deflectable angle α for different amplitude A with the same original length L of the upper friction layer. As the amplitude A increases, the deflection angle α can be increased. In this work, we conducted all experiments with an upper friction layer with $L = 19mm$, $\Delta L = 1mm$ and $A = 2.78mm$. As shown in Fig. 2c, the voltage of the upper friction layer is also different at different deflection angles α. As the deflection angle increases, the voltage is decreasing. Even when the voltage drops to the minimum, its magnitude is more than 50% of the maximum when the deflection angle α is the maximum deflection angle. Physical diagram of the voltage test with different deflection angles α is shown in Fig. S3.

The upper friction layer of the curved structure is deformed when it is compressed, and the voltage changes under different compression strains (Fig. 2d, e). We mounted the upper and lower friction layers on a linear motor and made them perform contact separation motion at a fixed speed (0.1 m/s). The physical diagram during the compression experiments can be seen in Fig. S4. Since the stiffness of the upper friction layer is much smaller than that of the lower friction layer, only the upper friction layer is deformed in the process of their contact. The voltage increases from 0% strain to 38% strain because the contact area of the upper and lower friction layers is increasing as the compressive strain increases. Here, the strain 0% refers to the case where the upper and lower friction layers are just in contact. When the strain is 44%, there is a slight drop in the voltage, which is because the contact area becomes smaller due to the buckling that occurs. As the strain increases from 44% to 71%, the contact area increases again and the voltage rises again.

To better analyze the mechanical behavior of the upper friction layer during the compression process. We simulated the deformation of the upper friction layer under different compression strains with FEA. The contact area between the upper friction layer and the lower friction layer is increasing from the initial state until the compression strain is 40% (Fig. 2f). By the time the compressive strain is 60%, the upper friction layer has been buckling at this time, but still continues to be compressed and the contact area continues to increase. The FEA results show the same behavior of compression, buckling, and recompression as the compression experiments. The yield point of the friction material FEP in the upper friction layer is 12 MPa. as can be seen in Fig. 2f, when the compression strain is 40%, the FEP film exceeds the yield point and enters a phase of deformation irreversibility. We investigated the force-strain curve of the upper friction layer with different parameters using finite elements. As shown in Fig. 2g, the compressive stiffness of the upper friction layer is increasing as the thickness of PI increases. As shown in Fig. 2h, the compressive stiffness of the upper friction layer is increasing with the increase of the upper friction layer amplitude A. As can be seen in Fig. 2g and h, there is an abrupt drop in force when the applied strain is between 40% and 50%, which is due to the buckling of the upper friction layer.

In order to drive Li-TENG even under micro force, we choose SLA with a lighter density of 1.13 g/cm^3 as the material for manufacturing the main bar. After the upper and lower friction layers come into contact, the main bar can continue to rotate around the supporting point because the bending stiffness of the main bar is not large. At this time, the main bar will bend and the contact area of the upper and lower friction layers will increase. Fig. 3a shows the Mises stress diagram at a rotation angle of 18.9 degrees after the bending of the main bar. The part with the most severe deformation is where the spring is installed (red dotted box). The magnified view of this part (Fig. 3b) shows that the Mises stress is a maximum of 38.4 MPa, while the stress strength of the SLA is 38 MPa. There is a risk of fracture of the main bar when the rotation angle exceeds 18.9 degrees. We investigated the relationship between the rotation angle and the endpoint force of the main bar, as shown in Fig. 3c, the endpoint force is increasing as the rotation angle increases. The endpoint force is as large as the compression force on the upper friction layer. The endpoint force at 18.9 degrees is 0.6 N, which is less than the compression force when the upper friction layer is buckling. Therefore, the main bar of this design can prevent the upper friction layer from buckling.

3.3. Output performance of Li-TENG

Then, we investigated the effect of the contact separation speed on the magnitude of the voltage of the Li-TENG. The Li-TENG was driven by a linear motor to study the performance of the Li-TENG at different speeds by setting the speed of the linear motor. The magnitude of the voltage is increasing as the speed increases (Fig. 4a). The experimental results are consistent with the theory. A fixed distance of travel is set for the upper friction layer using the linear motor, and without the blockage of the lower friction layer, the upper friction layer will continue to move forward after reaching the set position due to inertia. When the linear motor is moving at 0.001 m/s, we consider the upper friction layer to be in quasi-static motion and will not move out of the set position due to inertia. We define the position where the upper friction layer and the lower friction layer are just in contact as the 0 mm position under quasi-static motion. When the speed of the linear motor is 0.01 m/s, 0.03 m/s and 0.04 m/s, and the position of the lower friction layer is −4 mm, −20 mm and −30 mm respectively due to inertia, the upper and lower friction layers are just in contact, as shown in Fig. 4b. When the speed of the linear motor is constant, changing the position of the lower friction layer will change the magnitude of the voltage. As shown in Fig. 4b, for example, the voltage increases when the position of the lower friction layer is changed from the position of −30 mm, which is just in contact, up to the position of −4 mm, at 0.04 m/s. When the position of the lower friction layer rises from −4 to 5 mm, the magnitude of the voltage enters a plateau period and remains almost unchanged. When the position of the lower friction layer rises from 5 mm to 10 mm, there is a slight

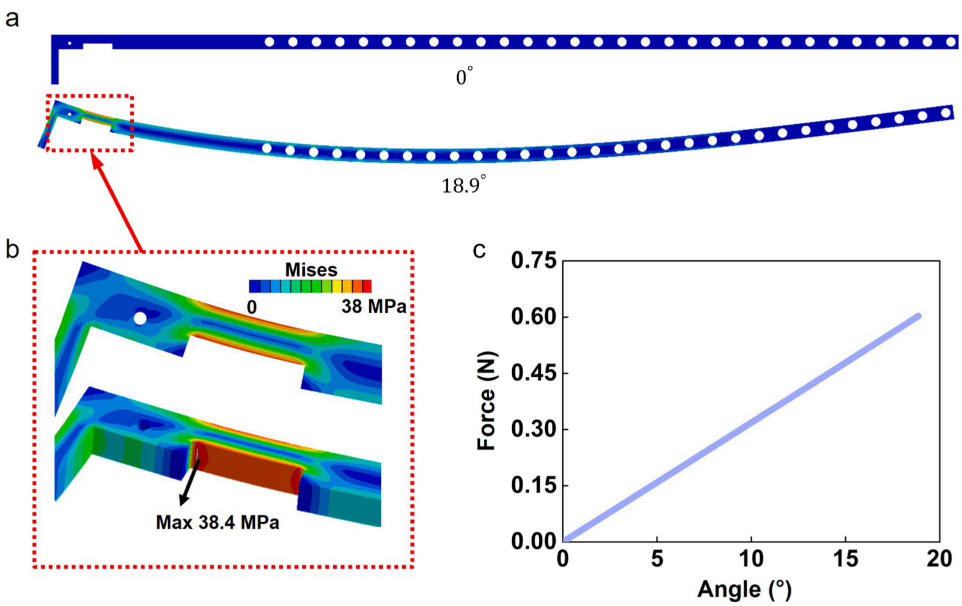

Fig. 3. FEA results of the main bar. Stress distributions of (a) the main bar and (b) the main bar local. (c) Force-angle curves of the main bar.

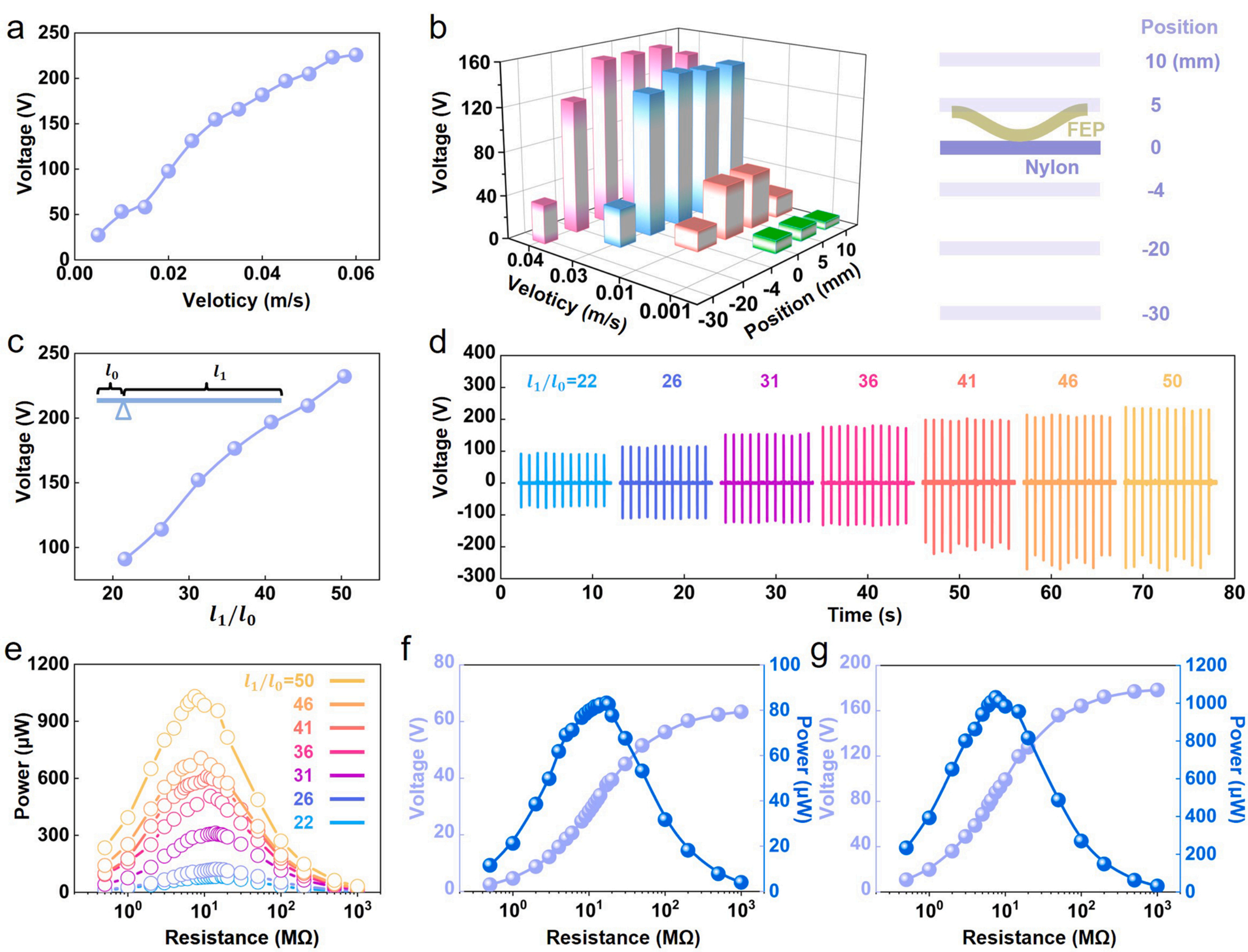

Fig. 4. Electrical measurements of Li-TENG. Voltage measurement at (a) different speeds and (b) different positions. (c) Voltage signal and (d) voltage waveform at different magnifications. (e) Power diagram at different magnifications. Voltage power diagram at (f) 22x magnification and (g) 50x magnification.

decrease in the voltage. During the change of the position of the lower friction layer, the voltage is maximum during the platform period.

We installed the upper friction layer at different positions of the main bar to study the effect of different magnifications on the magnitude of the voltage under the lever action. During the measurement at different magnifications, the position of the lower friction layer was adjusted to ensure that the maximum voltage appeared. The voltage increased from 91 V to 232 V when the magnification increased from 22 to 50 times (Fig. 4c, d), indicating that the voltage can be significantly increased by increasing the magnification under the design of the lever structure. We also investigated the effect of magnification on power and optimal impedance. As shown in Fig. 4e, the maximum power increases from 83 μW to 1031 μW and the optimum impedance decreases from 17 MΩ to 7.5 MΩ as the magnification increases from 22 to 50 times. Fig. 4f and g show the voltage power figure at 22 and 50 times of magnification, respectively.

3.4. Li-TENG for mechanical analysis and pulse measurement applications

Li-TENG is able to significantly increase the voltage by amplifying the speed, which is suitable for TENG with small displacement and weak signal. Pulse has a large force but small displacement, which is very suitable for Li-TENG application scenario. Moreover, pulse monitoring is very important in human health monitoring. We first analyze the force on the Li-TENG during pulse monitoring, as shown in Fig. 5a. The pulse has a force F_{pulse} on the front of the Li-TENG, which is used to drive the movement of the Li-TENG. the selection of the spring in the groove of the Li-TENG is important, which provides the spring force F_{spring}. The force analysis also includes the gravitational force G of the main bar of the Li-TENG and the electrostatic gravitational force $F_{electrostatic}$ between the upper and lower friction layers. The pulse is wrapped around a skin layer. The thicker the skin layer is, the more difficult it is for the pulse force F_{pulse} to be transmitted to the Li-TENG. In addition to overcoming the gravitational force G and the electrostatic gravitational force $F_{electrostatic}$, the spring has to compress the skin layer so that most of the pulse force F_{pulse} can be transferred to the Li-TENG. However, the spring force F_{spring} should not be too large, otherwise the pulse force F_{pulse} cannot overcome the spring force F_{spring} to drive the Li-TENG. At the same time, the spring needs to choose a suitable stiffness, too little stiffness will increase the volume of the Li-TENG, and too much stiffness will make the displacement of the upper friction layer too small.

The dynamics model of Li-TENG is the single degree-of-freedom (DOF) spring-mass-damper model, as shown in Fig. 5b. The equation of motion of this simple vibration model is

$$m\frac{d^2y}{dt^2} + c\frac{dy}{dt} + ky = F \tag{2}$$

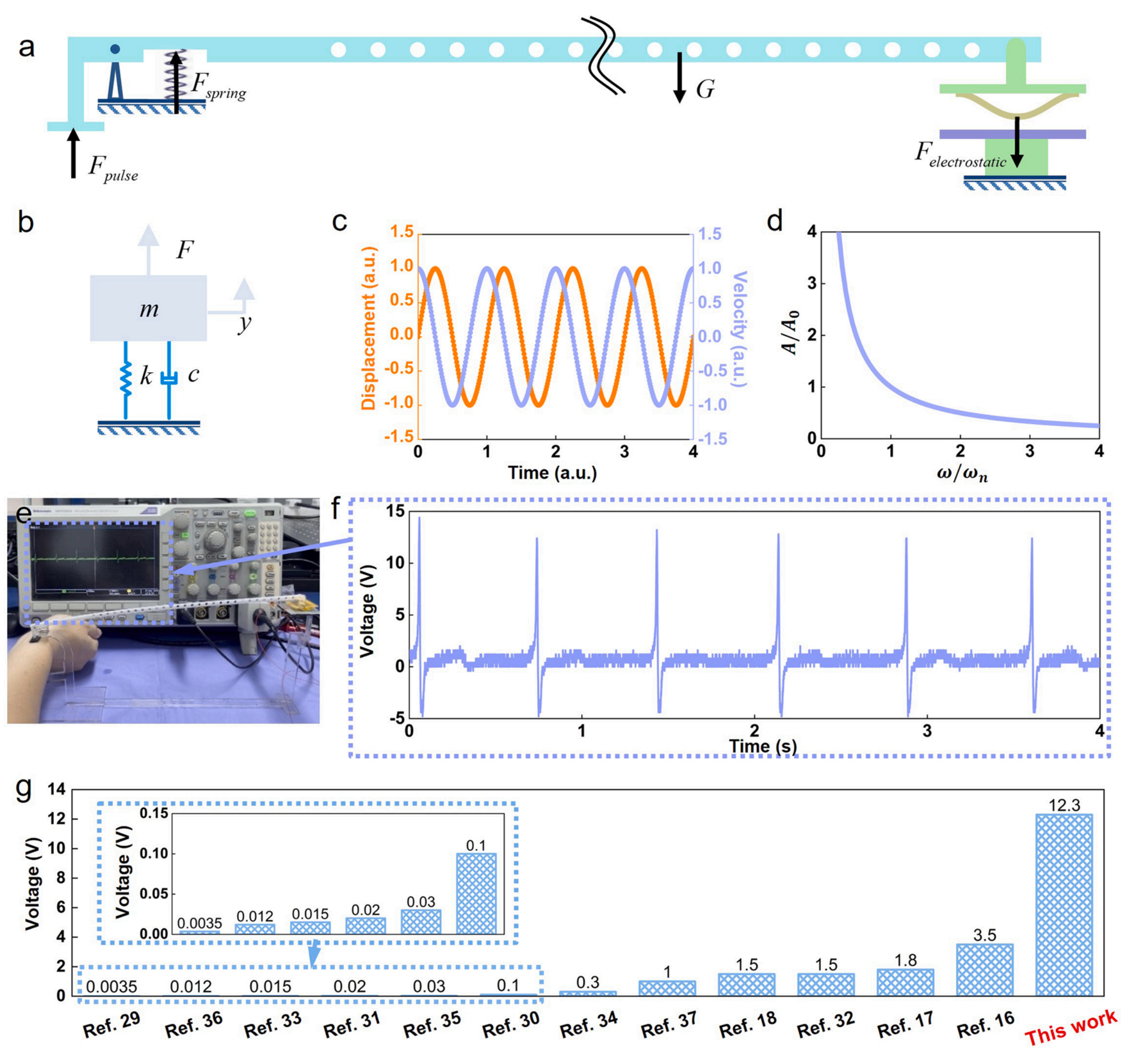

Fig. 5. Li-TENG for mechanical analysis and pulse measurement applications. (a) Force analysis of Li-TENG. (b) Kinetic model of Li-TENG. Theoretical (c) displacement-velocity-time and (d) amplitude ratio-intrinsic frequency ratio relationship of Li-TENG. (e) Physical and (f) signal diagrams of pulse measurement with Li-TENG. (g) Comparison of the pulse signal measured by Li-TENG with other literature.

where $y$denotes the sinusoidal movement of the upper friction layer center of mass. m denotes the mass of the backpack. The stiffness k and damping c are the equivalent spring constant and damping coefficient. The combined force suffered can be expressed as $F = A_0 m \sin(\omega t)$, where amplitude, radial frequency and time are given by A_0, $\omega$and t. The natural radial frequency of Li-TENG is given by $\omega_n = \sqrt{k/m}$. The steady-state response of the upper friction layer can be expressed as Eq. (3) below,

$$y = A \sin(\omega t - \phi) \tag{3}$$

$$\frac{dy}{dt} = A\omega \cos(\omega t - \phi) \tag{4}$$

where A is the amplitude of oscillation, ϕ is the relative phase shift of the oscillation. Solving Eq. (2) gives $A/A_0$and ϕ in Eqs. (5) and (6) below,

$$\frac{A}{A_0} = \sqrt{\frac{1 + 4\zeta^2\varpi^2}{(1 - \varpi^2)^2 + 4\zeta^2\varpi^2}} \tag{5}$$

$$\tan\phi = \frac{2\zeta\varpi^3}{1 - \varpi^2 + 4\zeta^2\varpi^2} \tag{6}$$

where the amplitude ratio is given by $\varpi = \omega/\omega_n$, and the damping ratio is given by$\zeta = c/2m\omega_n$. Fig. 5c illustrates the curves of displacement, velocity and time of the upper friction layer according to Eqs. (3) and (4). When the displacement of the upper friction layer is maximum, its velocity magnitude is 0. Therefore, we cannot place the position of the lower friction layer to the position where the upper and lower friction layers are just in contact. We should adjust the position of the lower friction layer to the middle of the movement of the upper friction layer, so that the relative velocity of the upper and lower friction layers when they are in contact is the maximum. Fig. 5d shows that the frequency of the driving end has a great influence on the amplitude of the upper friction layer according to Eq. (5). If the frequency of the drive end is large, the amplitude of the upper friction layer will be small. Therefore, Li-TENG is not suitable for voltage magnification under high frequency motion.

We monitored the pulse signal from the right radial artery with Li-TENG, and the physical picture of the test is shown in Fig. 5e. A video of the test procedure is in Movie S1. Fig. 5f shows the specific pulse signal. As shown in Fig. 5g [16–18,29–37], previous scholar has increased the signal output by surface preprocessing, and the pulse signal measured in this case was a maximum of 3.5 V [16], much smaller than the 12.3 V of this work. demonstrating the great role of the lever structure in signal magnification.

4. Conclusion

To summarize, we propose a new strategy to enhancement of the signal by increasing the charge transfer speed and develop a lever-inspired TENG. we investigate the electrical and mechanical properties of the curved friction layer under different compressive strains. As the magnification increases from 22 to 50 times, the voltage of Li-TENG increases from 91 V to 232 V. As self-powered pulse sensor, the Li-TENG measured a pulse signal of 12.3 V without surface microstructure treatment, which is much higher than other literature. This work shows great potential for improving the signal of contact-separation TENG-based self-powered sensors and energy harvesting devices.

CRediT authorship contribution statement

Y.S. and **Y.Y.** supervised the research and conceived the idea. **M.Z.**, **W.Z.** and **T.Z.** carried out the device fabrication and the performance measurement. **M.Z.**, **Y.S.** and **Y.Y.** analyzed the data and co-wrote the manuscript. All authors read and revised the manuscript.

Declaration of Competing Interest

The authors declare that they have no known competing financial interests or personal relationships that could have appeared to influence the work reported in this paper.

Acknowledgements

This work was supported by the National Key R&D Project from the Minister of Science and Technology in China (Grant No. 2021YFA1201604), the National Natural Science Foundation of China (Grant No. 52072041), the Beijing Natural Science Foundation (Grant No. JQ21007), the University of Chinese Academy of Sciences (Grant No. Y8540XX2D2), Y.S. gratefully acknowledges the support from the National Natural Science Foundation of China (No. 12172359), Beijing Municipal Science and Technology Commission (Z191100002019010), Beijing Municipal Natural Science Foundation (No. 2202066), Key Research Program of Frontier Sciences of the Chinese Academy of Sciences (ZDBS-LY-JSC014) and CAS Interdisciplinary Innovation Team (JCTD-2020-03).

Appendix A. Supporting information

Supplementary data associated with this article can be found in the online version at doi:10.1016/j.nanoen.2022.107159.

References

[1] F.R. Fan, Z.Q. Tian, Z.L. Wang, Flexible triboelectric generator, Nano Energy 1 (2012) 328–334.
[2] M. Pan, C.G. Yuan, X.R. Liang, J. Zou, Y. Zhang, C. Bowen, Triboelectric and piezoelectric nanogenerators for future soft robots and machines, iScience 23 (2020), 101682.
[3] S.H. Wang, X. Wang, Z.L. Wang, Y. Yang, Efficient scavenging of solar and wind energies in a smart city, ACS Nano 10 (2016) 5696–5700.
[4] S.H. Wang, L. Lin, Y.N. Xie, Q.S. Jing, S.M. Niu, Z.L. Wang, Sliding-triboelectric nanogenerators based on in-plane charge-separation mechanism, Nano Lett. 13 (2013) 2226–2233.
[5] G. Zhu, J. Chen, Y. Liu, P. Bai, Y.S. Zhou, Q.S. Jing, C.F. Pan, Z.L. Wang, Linear-grating triboelectric generator based on sliding electrification, Nano Lett. 13 (2013) 2282–2289.
[6] X. Wang, Y. Yang, Effective energy storage from a hybridized electromagnetic-triboelectric nanogenerator, Nano Energy 32 (2017) 36–41.
[7] Q. Jiang, B. Chen, Y. Yang, Wind-driven triboelectric nanogenerators for scavenging biomechanical energy, ACS Appl. Energy Mater. 1 (2018) 4269–4276.
[8] X. Liu, K. Zhao, Y. Yang, Effective polarization of ferroelectric materials by using a triboelectric nanogenerator to scavenge wind energy, Nano Energy 53 (2018) 622–629.
[9] T. Quan, Y.C. Wu, Y. Yang, Hybrid electromagnetic-triboelectric nanogenerator for harvesting vibration energy, Nano Res. 8 (2015) 3272–3280.
[10] B. Chen, N.N. Yang, Q. Jiang, W.S. Chen, Y. Yang, Transparent triboelectric nanogenerator-induced high voltage pulsed electric field for a self-powered handheld printer, Nano Energy 44 (2018) 468–475.
[11] Q. Tang, M.H. Yeh, G.L. Liu, S.M. Li, J. Chen, Y. Bai, L. Feng, M.H. Lai, K.C. Ho, H. Y. Guo, C.G. Hu, Whirligig-inspired triboelectric nanogenerator with ultrahigh specific output as reliable portable instant power supply for personal health monitoring devices, Nano Energy 47 (2018) 74–80.
[12] X. Chen, L.X. Gao, J.F. Chen, S. Lu, H. Zhou, T.T. Wang, A.B. Wang, Z.F. Zhang, S. F. Guo, X.J. Mu, Z.L. Wang, Y. Yang, A chaotic pendulum triboelectric-electromagnetic hybridized nanogenerator for wave energy scavenging and self-powered wireless sensing system, Nano Energy 69 (2020), 104440.
[13] X.D. Zhong, Y. Yang, X. Wang, Z.L. Wang, Rotating-disk-based hybridized electromagnetic-triboelectric nanogenerator for scavenging biomechanical energy as a mobile power source, Nano Energy 13 (2015) 771–780.
[14] K.M. Yao, Y.M. Liu, D.F. Li, J.H. He, J.Y. Li, R.H.W. Lam, Z.Q. Xie, L.D. Wang, X. G. Yu, Mechanics designs-performance relationships in epidermal triboelectric nanogenerators, Nano Energy 76 (2020), 105017.
[15] Y. Yang, Y.S. Zhou, H.L. Zhang, Y. Liu, S.M. Lee, Z.L. Wang, A single-electrode based triboelectric nanogenerator as self-powered tracking system, Adv. Mater. 25 (2013) 6594–6601.
[16] K.Y. Meng, J. Chen, X.S. Li, Y.F. Wu, W.J. Fan, Z.H. Zhou, Q. He, X. Wang, X. Fan, Y.X. Zhang, J. Yang, Z.L. Wang, Flexible weaving constructed self-powered pressure sensor enabling continuous diagnosis of cardiovascular disease and measurement of cuffless blood pressure, Adv. Funct. Mater. 29 (2019), 1806388.
[17] Z.M. Lin, J. Chen, X.S. Li, Z.H. Zhou, K.Y. Meng, W. Wei, J. Yang, Z.L. Wang, Triboelectric nanogenerator enabled body sensor network for self-powered human heart-rate monitoring, ACS Nano 11 (2017) 8830–8837.

[18] H. Ouyang, J.J. Tian, G.L. Sun, Y. Zou, Z. Liu, H. Li, L.M. Zhao, B.J. Shi, Y.B. Fan, Y. F. Fan, Z.L. Wang, Z. Li, Self-powered pulse sensor for antidiastole of cardiovascular disease, Adv. Mater. 29 (2017), 1703456.
[19] L.X. Gao, X. Chen, S. Lu, H. Zhou, W.B. Xie, J.F. Chen, M.K. Qi, H. Yu, X.J. Mu, Z. L. Wang, Y. Yang, Enhancing the Output Performance of Triboelectric Nanogenerator via Grating-Electrode-Enabled Surface Plasmon Excitation, Adv. Energy Mater. 9 (2019), 1902725.
[20] P. Bai, G. Zhu, Z.H. Lin, Q.S. Jing, J. Chen, G. Zhang, J. Ma, Z.L. Wang, Integrated multi layered triboelectric nanogenerator for harvesting biomechanical energy from human motions, ACS Nano 7 (2013) 3713–3719.
[21] T.X. Xiao, X. Liang, T. Jiang, L. Xu, J.J. Shao, J.H. Nie, Y. Bai, W. Zhong, Z.L. Wang, Spherical triboelectric nanogenerators based on spring-assisted multilayered structure for efficient water wave energy harvesting, Adv. Funct. Mater. 28 (2018), 1802634.
[22] H. Ryu, H.M. Park, M.K. Kim, B. Kim, H.S. Myoung, T.Y. Kim, H.J. Yoon, S.S. Kwak, J. Kim, T.H. Hwang, E.K. Choi, S.W. Kim, Self-rechargeable cardiac pacemaker system with triboelectric nanogenerators, Nat. Commun. 12 (2021) 4374.
[23] X. Hang, T. Jiang, G.X. Liu, T.X. Xiao, L. Xu, W. Li, F.B. Xi, C. Zhang, Z.L. Wang, Triboelectric nanogenerator networks integrated with power management module for water wave energy harvesting, Adv. Funct. Mater. 29 (2019), 1807241.
[24] G.L. Liu, H.Y. Guo, L. Chen, X. Wang, D.P. Wei, C.G. Hu, Double-induced-mode integrated triboelectric nanogenerator based on spring steel to maximize space utilization, Nano Res. 9 (2016) 3355–3363.
[25] H.M. Wang, L. Xu, Y. Bai, Z.L. Wang, Pumping up the charge density of a triboelectric nanogenerator by charge-shuttling, Nat. Commun. 11 (2020) 4203.
[26] Y.K. Liu, W.L. Liu, Z. Wang, W.C. He, Q. Tang, Y. Xi, X. Wang, H.Y. Guo, C.G. Hu, Quantifying contact status and the air-breakdown model of charge-excitation triboelectric nanogenerators to maximize charge density, Nat. Commun. 11 (2020) 1599.
[27] L. Cheng, Q. Xu, Y.B. Zheng, X.F. Jia, Y. Qin, A self-improving triboelectric nanogenerator with improved charge density and increased charge accumulation speed, Nat. Commun. 9 (2018) 3773.
[28] W.L. Liu, Z. Wang, G. Wang, G.L. Liu, J. Chen, X.J. Pu, Y. Xi, X. Wang, H.Y. Guo, C. G. Hu, Z.L. Wang, Integrated charge excitation triboelectric nanogenerator, Nat. Commun. 10 (2019) 1426.
[29] W. Xiong, K. Hu, Z. Li, Y.X. Jiang, Z.G. Li, Z. Li, X.W. Wang, A wearable system based on core-shell structured peptide-Co9S8 supercapacitor and triboelectric nanogenerator, Nano Energy 66 (2019), 104149.
[30] Q.Q. Niu, L. Huang, S.S. Lv, H.L. Shao, S.N. Fan, Y.P. Zhang, Pulse-driven bio-triboelectric nanogenerator based on silk nanoribbons, Nano Energy 74 (2020), 104837.
[31] S.W. Chen, N. Wu, S.Z. Lin, J.J. Duan, Z.S. Xu, Y. Pan, H.B. Zhang, Z.H. Xu, L. Huang, B. Hu, J. Zhou, Hierarchical elastomer tuned self-powered pressure sensor for wearable multifunctional cardiovascular electronics, Nano Energy 70 (2020), 104460.
[32] W.J. Fan, Q. He, K.Y. Meng, X.L. Tan, Z.H. Zhou, G.Q. Zhang, J. Yang, Z.L. Wang, Machine-knitted washable sensor array textile for precise epidermal physiological signal monitoring, Sci. Adv. 6 (2020) eaay2840.
[33] X. Peng, K. Dong, C.Y. Ye, Y. Jiang, S.Y. Zhai, R.W. Cheng, D. Liu, X.P. Gao, J. Wang, Z.L. Wang, A breathable, biodegradable, antibacterial, and self-powered electronic skin based on all-nanofiber triboelectric nanogenerators, Sci. Adv. 6 (2020) eaba9624.
[34] Z.X. Liu, Z.Z. Zhao, X.W. Zeng, X.L. Fu, Y. Hu, Expandable microsphere-based triboelectric nanogenerators as ultrasensitive pressure sensors for respiratory and pulse monitoring, Nano Energy 59 (2019) 295–301.
[35] Y.C. Lai, J. Deng, S.L. Zhang, S. Niu, H. Guo, Z.L. Wang, Single-thread-based wearable and highly stretchable triboelectric nanogenerators and their applications in cloth-based self-powered human-interactive and biomedical sensing, Adv. Funct. Mater. 27 (2017), 1604462.
[36] K. Dong, Z.Y. Wu, J.A. Deng, A.C. Wang, H.Y. Zou, C.Y. Chen, D.M. Hu, B.H. Gu, B. Z. Sun, Z.L. Wang, A stretchable yarn embedded triboelectric nanogenerator as electronic skin for biomechanical energy harvesting and multifunctional pressure sensing, Adv. Mater. 30 (2018), 1804944.
[37] J. Yang, J. Chen, Y.J. Su, Q.S. Jing, Z.L. Li, F. Yi, X.N. Wen, Z.N. Wang, Z.L. Wang, Eardrum-inspired active sensors for self-powered cardiovascular system characterization and throat-attached anti-interference voice recognition, Adv. Mater. 27 (2015) 1316.
[38] S.M. Niu, S.H. Wang, L. Lin, Y. Liu, Y.S. Zhou, Y.F. Hu, Z.L. Wang, Theoretical study of contact-mode triboelectric nanogenerators as an effective power source, Energy Environ. Sci. 6 (2013) 3576–3583.
[39] S.H. Wang, L. Lin, Z.L. Wang, Nanoscale triboelectric-effect-enabled energy conversion for sustainably powering portable electronics, Nano Lett. 12 (2012) 6339–6346.
[40] J. Song, Y. Huang, J. Xiao, S. Wang, K.C. Hwang, H.C. Ko, D.H. Kim, M. P. Stoykovich, J.A. Rogers, Mechanics of noncoplanar mesh design for stretchable electronic circuits, J. Appl. Phys. 105 (2009), 123516.
[41] Y.W. Su, J. Wu, Z.C. Fan, K.C. Hwang, J.Z. Song, Y.G. Huang, J.A. Rogers, Postbuckling analysis and its application to stretchable electronics, J. Mech. Phys. Solids 60 (2012) 487–508.

Maoyi Zhang is now pursuing his Ph.D. degree in Institute of Mechanics, Chinese Academy of Sciences, China. He received her bachelor's degree in Engineering Mechanics from Dalian University of Technology in 2017. His current research interests include flexible sensors and energy harvesters.

Wenxuan Zhu is studying for a master's degree at Guangxi University in the research group of Professor Ya Yang. She obtained her bachelor's degree in applied chemistry from China University of Petroleum (East China) in 2019. Her current research interest is triboelectric nanogenerator.

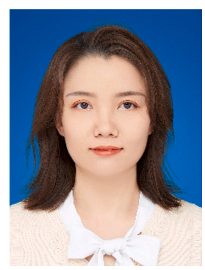

Tongtong Zhang is now pursuing her Ph.D. degree in the research group of Professor Ya Yang at Beijing Institute of Nanoenergy and Nanosystems, Chinese Academy of Sciences. She received her bachelor's degree in Chemical Engineering and Technology from Guangxi University in 2018. Her current interests focus on self-powered sensors.

Prof. Yewang Su received his Ph.D. from Tsinghua University, Beijing, China. He is currently a professor at Institute of Mechanics, Chinese Academy of Sciences, China. His research focuses on flexible and stretchable sensors in the field of sensing the curvature, large strain, and pressure et al. He is now finding the new application of flexible and stretchable sensors on wearable devices and the intelligent industry. He has been published more than 70 SCI papers in peer reviewed high-level scientific journals and held more than 20 patents in his research area.

Prof. Ya Yang received his Ph.D. in Materials Science and Engineering from University of Science and Technology Beijing, China. He is currently a professor at Beijing Institute of Nanoenergy and Nanosystems, Chinese Academy of Sciences, China. His main research interests focus on ferroelectric materials and devices for energy conver-sion, self-powered sensing, and some new physical effects. He has published one book and more than 190 SCI academic papers in Science Advances and other journals. These papers have been cited by more than 12000 times, and the corresponding H-index is 65. He is the Editor-in-Chief of Nanoenergy Advances and is the editorial committee member of InfoMat, Nano-Micro Letters, Nanoscale, iScience, Nanoscale Advances, and some other journals. He is the Guest Editor of Research, iScience, Nanomaterials, and Energies. Details can be found at: http://www.researcherid.com/rid/A-7219–2016.